Superhigh Uniform Magnetic Cr Substitution in a 2D Mo_2C Superconductor for a Macroscopic-Scale Kondo Effect

Chuan Xu, Zhen Liu, Zongyuan Zhang, Zhibo Liu, Jingyin Li, Minghu Pan,* Ning Kang,* Hui-Ming Cheng, and Wencai Ren*

Substitutional doping provides an effective strategy to tailor the properties of 2D materials, but it remains an open challenge to achieve tunable uniform doping, especially at high doping level. Here, uniform lattice substitution of a 2D Mo_2C superconductor by magnetic Cr atoms with controlled concentration up to ≈46.9 at% by chemical vapor deposition and a specifically designed Cu/Cr/Mo trilayer growth substrate is reported. The concentration of Cr atoms can be easily tuned by simply changing the thickness of the Cr layer, and the samples retain the original structure of 2D Mo_2C even at a very high Cr concentration. The controlled uniform Cr doping enables the tuning of the competition of the 2D superconductor and the Kondo effect across the whole sample. Transport measurements show that with increasing Cr concentration, the superconductivity of the 2D Cr-doped Mo_2C crystals disappears along with the emergence of the Kondo effect, and the Kondo temperature increases monotonously. Using scanning tunneling microscopy/spectroscopy, the mechanism of the doping level effect on the interplay and evolution between superconductivity and the Kondo effect is revealed. This work paves a new way for the synthesis of 2D materials with widely tunable doping levels, and provides new understandings on the interplay between superconductivity and magnetism in the 2D limit.

2D materials provide many opportunities for exploring new physics and various intriguing applications.[1–3] Doping as an effective strategy has been widely used to tailor the properties of 2D materials, such as graphene[4] and transition metal dichalcogenides (TMDCs),[5,6] for the applications in electronics, optoelectronics, electrocatalysis, and energy storage

and conversion. It has been demonstrated that introducing dopants in 2D materials can improve the electrical conductivity and catalytic activity,[7,8] tune the bandgap and work function,[9,10] and introduce superconductivity and magnetism.[11,12] For the doped 2D materials, the properties are strongly depended on the doping species and concentration. Therefore, it is critical to develop a reliable synthetic method to control doping for specific applications.

Tuning the magnetic doping in 2D superconductors is essentially for exploring new electronic phases in the 2D limit and developing spintronic devices.[13–16] A combination of the superconducting and magnetic interactions in electronic systems give rise to a rich variety of quantum phenomena,[17,18] including rich spectra of Yu–Shiba–Rusinov (YSR) states,[19] long-range magnetic bound states,[20] and quantum phase transitions between different magnetic ground states.[21] Recently, 2D hybrid superconductor–magnetic impurities systems have attracted intense interest in the realization of topological superconductivity and Majorana modes.[22,23] However, previous studies of magnetic doping in 2D superconductors are mainly based on local magnetic adatom doping on the surface of 2D superconductor, and the samples suffer from inhomogeneous properties and poor environmental stability.

Dr. C. Xu, Dr. Z. Liu, Prof. H.-M. Cheng, Prof. W. Ren
Shenyang National Laboratory for Materials Science
Institute of Metal Research
Chinese Academy of Sciences
Shenyang 110016, P. R. China
E-mail: wcren@imr.ac.cn

Dr. Z. Liu, J. Li, Prof. N. Kang
Key Laboratory for the Physics and Chemistry of Nanodevices
and Department of Electronics
Peking University
Beijing 100871, P. R. China
E-mail: nkang@pku.edu.cn

Dr. Z. Zhang, Prof. M. Pan
School of Physics
Huazhong University of Science and Technology
Wuhan 430074, P. R. China
E-mail: minghupan@hust.edu.cn

Dr. Z. Zhang
Key Laboratory of Structure and Functional Regulation of Hybrid
Materials of Ministry of Education
Institutes of Physical Science and Information Technology
Anhui University
Hefei 230601, China

Prof. M. Pan
School of Physics and Information Technology
Shaanxi Normal University
Xi'an 710119, China

Prof. H.-M. Cheng, Prof. W. Ren
School of Materials Science and Engineering
University of Science and Technology of China
Shenyang 110016, P. R. China

Prof. H.-M. Cheng
Shenzhen Geim Graphene Center
Tsinghua-Berkeley Shenzhen Institute (TBSI)
Tsinghua University
Shenzhen 518055, P. R. China

**ADVANCED
SCIENCE NEWS**

www.advancedsciencenews.com

**ADVANCED
MATERIALS**

www.advmat.de

With the development of synthetic techniques, graphene and various 2D TMDCs doped with substitutional metal atoms in the lattice have been synthesized, as summarized in Table S1 of the Supporting Information. However, few of high level substitutional doping (over 20 at%) has been reported and, more importantly, phase segregation and structure transformation occur once the percentage of substitutional atoms are more than a critical value.[6] So far, it still remains an open challenge to achieve uniform substitutional doping of 2D materials, especially for high doping level. Here, we report uniformly magnetic Cr lattice substitution in 2D Mo_2C superconductors with controlled Cr content up to 46.9 at% by chemical vapor deposition (CVD) with a

specifically designed trilayer growth substrate, which enables the tuning of the competition of the superconductivity and the Kondo effect in the whole sample for devices.

Figure 1a–c shows the schematic of the growth of 2D substitutional Cr-doped Mo_2C crystals, in which a trilayer Cu/Cr/Mo foil was used as the growth substrate and methane as the carbon source. The Cu/Cr/Mo substrate was first annealed at 1070 °C sufficiently under H_2 atmosphere, which enables the formation of a homogeneous Cr–Mo alloy sandwiched between Cu and Mo foils (Figure 1b). Then, the Cu/Cr–Mo/Mo substrate was heated to 1090 °C to grow Cr-doped 2D Mo_2C on liquid Cu surface under H_2 and CH_4. Here, the liquid Cu layer acted as a diffusion channel of Cr and Mo atoms because of their low
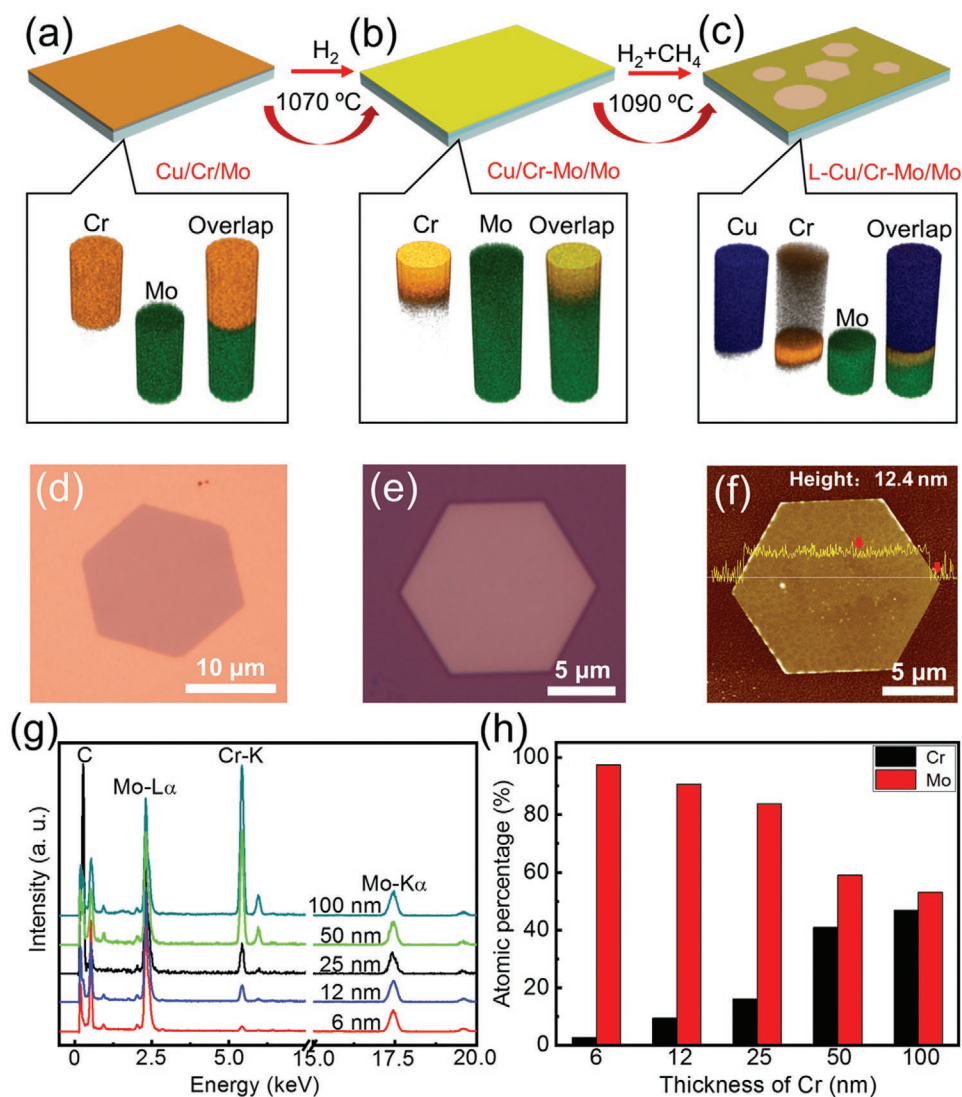

Figure 1. Fabrication of 2D Cr-doped Mo_2C crystals with controlled Cr concentrations. a–c) Schematic of the growth process of ultrathin Cr-doped Mo_2C crystals by CVD, and the reconstructed 3D TOF-SIMS images of the substrate in each stage are shown below. It can be found that the Cr film deposited on the surface of Mo foil (a) was transformed into homogeneous Cr–Mo alloy after annealing (b). When the substrate was heated to 1090 °C, Cr and Mo atoms diffused through liquid Cu onto the surface and reacted with the C atoms from the decomposition of CH_4 to form 2D Cr-doped Mo_2C crystals (c). d) Optical image of a hexagonal Cr-doped Mo_2C crystal grown with 100 nm thick Cr film. e,f) Optical image (e) and the corresponding AFM image (f) of a 12.4 nm thick Cr-doped Mo_2C crystal transferred on SiO_2/Si substrate. g) EDS spectra of the 2D Cr-doped Mo_2C crystals grown on Cu/Cr/Mo substrates, in which δ (Cr) is 6 nm (red), 12 nm (blue), 25 nm (black), 50 nm (green), and 100 nm (cyan), respectively. h) The corresponding atomic fractions of Cr and Mo elements in the samples in (g), showing an increase of Cr fraction with δ (Cr).

solubility in Cu and the absence of Cr–Cu and Mo–Cu intermetallic compound (Figure 1c).[24,25] The Cr–Mo alloy ensures the supply of Cr and Mo atoms with a specific mole ratio during growth, which is the key for the formation of uniform Cr-doped Mo_2C through reacting with the carbon atoms supplied by the decomposition of methane. Figure 1d–f shows the typical Cr-doped 2D Mo_2C crystals. Optical and atomic force microscopy (AFM) measurements show that all the crystals have regular shape, a thickness of 5–20 nm and smooth surface.

Importantly, we can easily tune the concentration of Cr in Mo_2C crystals by changing the thickness of the Cr film, δ (Cr). Figure 1g shows the energy-dispersive X-ray spectroscopy (EDS) spectra of the Mo_2C crystals grown with different thickness of Cr films. For comparison, all the spectra were normalized by the signal of Mo element. Note that the intensity of Cr-K peak (I_{Cr-K}) increases monotonously with δ (Cr). The extracted atomic fraction of Cr is 2.7, 9.4, 16.1, 40.9, and 46.9 at%, respectively, in the crystals that were grown with δ (Cr) of 6, 12, 25,

50, and 100 nm (Figure 1h). In addition, the nucleation density of the crystals decreases with increasing δ (Cr). At δ (Cr) of 500 nm, no any regular crystals are found on the whole substrate (Figure S1, Supporting Information). Interestingly, the shape of the crystals can also be regulated with δ (Cr). Shape diversity decreases with δ (Cr). Without the use of Cr layer, six kinds of shapes are observed dominated with octagons. At δ (Cr) $\geq$ 25 nm, only hexagonal and dodecagonal crystals are formed and the percentage of hexagonal crystals decreases with δ (Cr). These results suggest that the use of Cr significantly affects the nucleation and growth of 2D Mo_2C crystals.

EDS mapping was performed to characterize the Cr distribution in 2D Mo_2C crystals. Notably, Mo, C, and Cr are uniformly distributed across the whole sheet with 46.9 at% Cr (**Figure 2**a–d). Time of flight secondary ion mass spectrometry (TOF-SIMS) was further used to identify the lateral and depth distribution of various elements (Figure 2e–h). A Bi positive-ion-beam was used to take the signals from the elements on the surface to
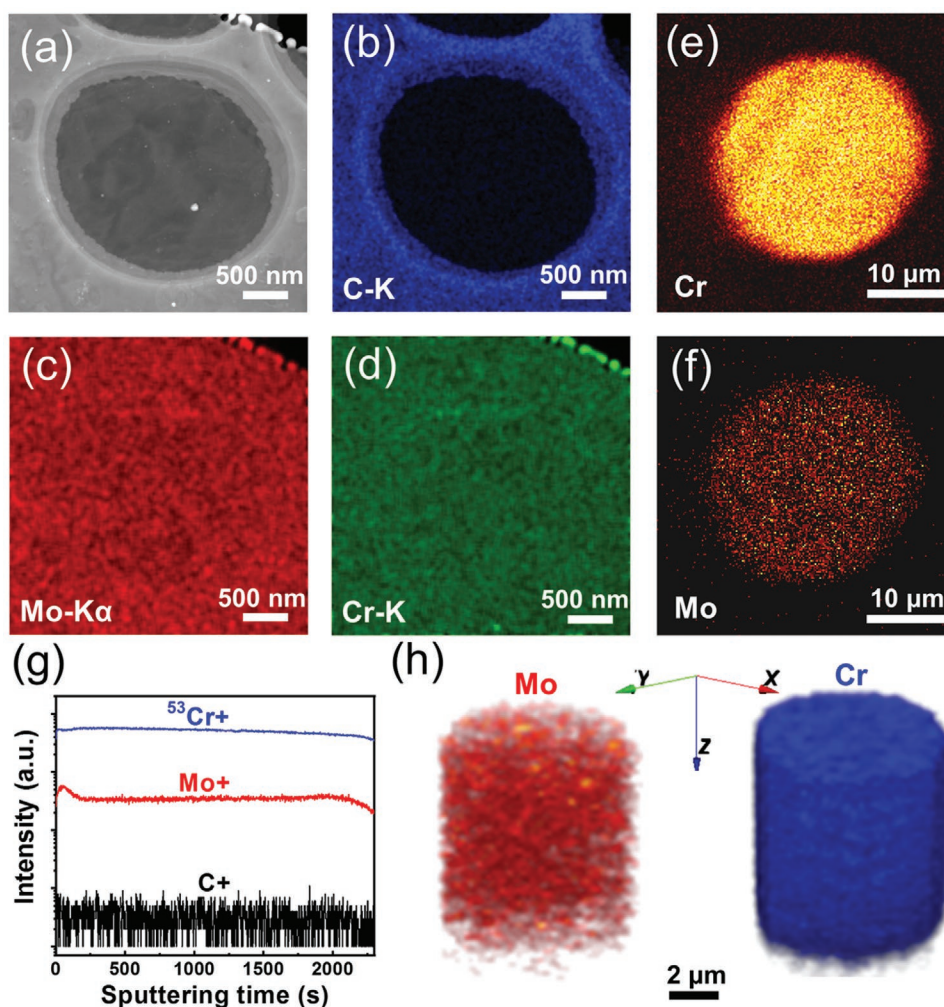

Figure 2. Cr distribution characterizations in 2D Cr-doped Mo_2C crystals. a–d) Low-magnification HAADF-STEM image of a 2D Mo_2C crystal with 46.9 at% Cr (a) and the corresponding EDS elemental mappings of C-K (b), Mo-Kα (c), and Cr-K (d) lines across the whole sheet, showing the uniform distribution of C, Mo, and Cr. e,f) SIMS maps of Mo (e) and Cr positive ions (f) of a 2D Mo_2C crystal with 46.9 at% Cr grown on Cu/Cr(100 nm)/Mo substrate. g) Depth distribution of Cr (red line), Mo (blue line), and C (black line) elements along the thickness direction of the crystal in (e) and (f), respectively. h) The corresponding 3D simulation of the distribution of Mo and Cr, respectively.

2002825 (3 of 10)

**ADVANCED
SCIENCE NEWS**

www.advancedsciencenews.com

**ADVANCED
MATERIALS**

www.advmat.de

provide lateral element distribution. An oxygen-ion-beam was used to etch the sample layer by layer to collect the signals from the inner atoms and thus the depth distribution of elements was obtained by prolonging the sputtering time. Figure 2e, f shows that both Mo and Cr have very uniform distribution along the lateral direction, consistent with EDS mapping results. Furthermore, it is worth noting that Mo, C, and Cr remain almost the same SIMS intensity with the depth until the sample was etched away (Figure 2g), suggesting the uniform depth distribution of Mo, C, and Cr. The reconstructed 3D TOF-SIMS images of Mo and Cr clearly show the uniform distribution of both Mo and Cr within the whole crystal (Figure 2h). The signal of C is too weak to reconstruct a well-defined 3D image. Raman mapping

provides another evidence on the uniform distribution of Cr in the samples with 46.9 at% Cr at the microscale (Figure S2, Supporting Information). Similarly, the samples with Cr content of 2.7, 9.4, 16.1, and 40.9 at% also show uniform distributions of Cr and Mo, demonstrating that this CVD process is effective for the growth of uniform Cr-doped Mo_2C with controlled doping concentration (Figures S3–S6, Supporting Information).

We further used selected-area electron diffraction (SAED), high-resolution scanning transmission electron microscopy (HR-STEM) and atomic resolution EDS mappings to characterize the structure and quality of the 2D Cr-doped Mo_2C crystals. **Figure 3**a,b shows a bright-field TEM image and the corresponding SAED pattern of an ultrathin hexagonal Mo_2C with
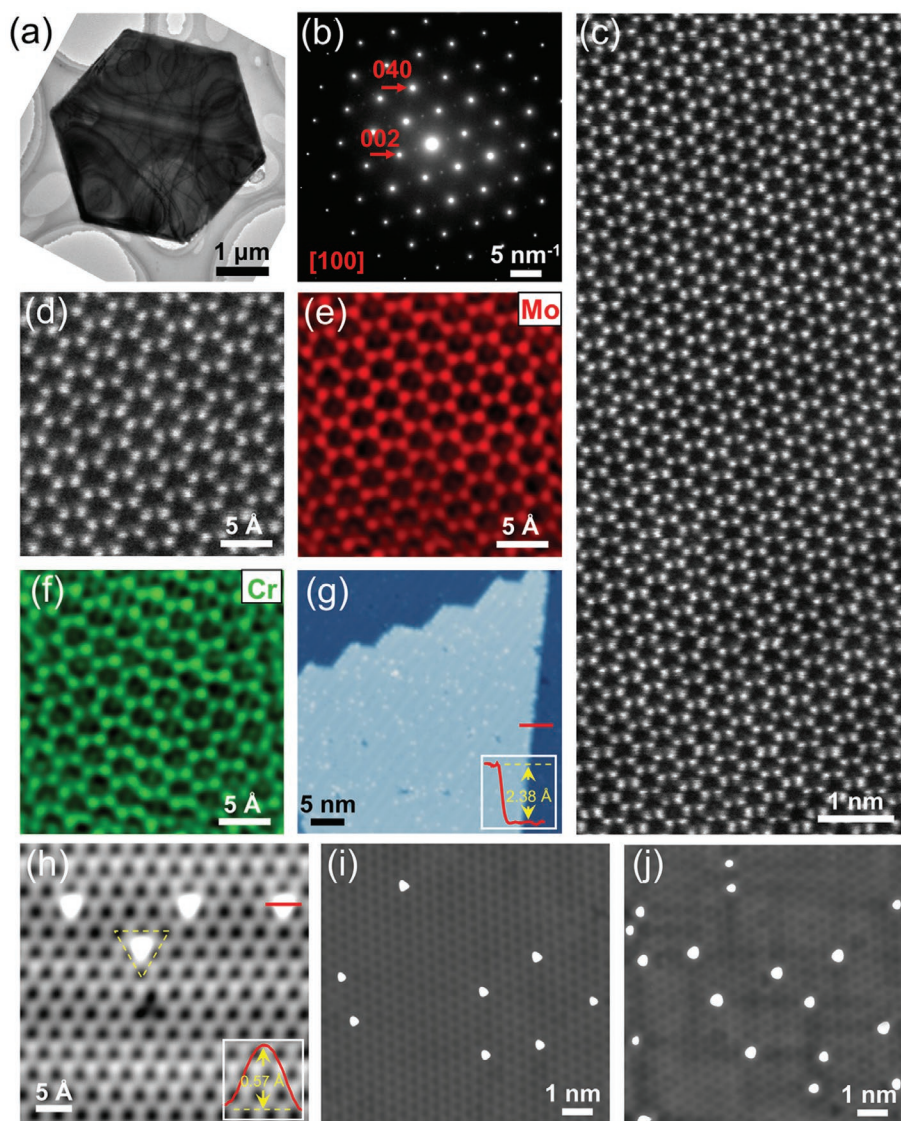

Figure 3. Atomic-level structure characterizations of 2D Cr-doped Mo_2C crystals. a,b) Low-magnification TEM image (a) and the corresponding SAED pattern (b) of a typical hexagonal Cr-doped Mo_2C crystal. c) Atomic-level HAADF-STEM image of a 2D Mo_2C crystal with 46.9 at% Cr. d–f) Atomic-level STEM image (d) and the corresponding EDS mappings of Mo-Kα (e) and Cr-K (f). g) STM image of a 9.4 at% Cr-doped Mo_2C (V_s = 0.5 V, I_t = 0.1 nA, T = 4.2 K). Many bright spots are observed on the flat terraces, which can be assigned as Cr-doped sites. Inset: the height profile along the red line, indicating that the step height (2.38 Å) fits well with the thickness of a single Mo–C–Mo layer (2.36 Å). h) Magnified STM view of the 2D Cr-doped Mo_2C crystal (V_s = 10 mV, I_t = 0.25 nA, T = 4.2 K). The Cr dopants are identified at atomic scale, showing regular triangular shapes. i,j) STM images of 2.7 at% (i) and 9.4 at% (j) Cr-doped Mo_2C crystals, clearly showing different densities of Cr dopants.

**ADVANCED
SCIENCE NEWS**

www.advancedsciencenews.com

**ADVANCED
MATERIALS**

www.advmat.de

46.9 at% Cr. Based on the SAED pattern, the crystal has a typically orthorhombic crystal structure with lattice constants of $b = 0.591$ nm and $c = 0.515$ nm, which are the same as the undoped pristine 2D Mo_2C crystal.[26] The atomic-level HAADF-STEM image further confirms that such Mo_2C with 46.9 at% Cr still has the same crystal structure as the pristine α-Mo_2C crystal(Figure 3c; Figure S7a, Supporting Information). Moreover, the crystal has a highly crystalline quality. The similar brightness of each atomic column suggests no element segregation and second phase even at such high Cr doping level (Figure 3c). Atomic resolution EDS mappings confirm the uniform distribution of Cr in Mo_2C crystals (Figure 3d–f). Importantly, the sites of Cr are completely overlapped with those of Mo, which means Cr atoms substitute a part of Mo atoms in Mo_2C lattice. The unchanged lattice constant is attributed to the similar size of Cr and Mo atoms. The 16.1 at% Cr-doped Mo_2C crystal shows similar structure characteristics (Figures S7b and S8, Supporting Information), and the consistency between the HAADF-STEM image and simulation result providing solid evidence to support Cr lattice substitution in Mo_2C (Figures S8 and S9, Supporting Information).

To further identify the Cr dopants in the lattice of Mo_2C surface layer, we also carried out scanning tunneling microscopy (STM) measurements. Low bias voltage was used to to get a good atomic resolution of the Cr atoms (Figure S10, Supporting Information). Figure 3g shows an STM image of a 2D Mo_2C crystal doped with 9.4 at% Cr. From this image, terraces with a step height of 2.38 Å can be found (inset), which is consistent with the thickness of a Mo–C–Mo layer.[27,28] Note that many bright protrusions on the flat terraces can be seen clearly in the magnified view (Figure 3h). By contrast, no protrusions are found in the undoped sample. Therefore, the only origin of these protrusions is Cr doping, which is about 0.5 Å high (inset of Figure 3h; Figure S11, Supporting Information) with a diameter of ≈ 4 Å. Note that these protrusions are anisotropic with a triangular configuration, indicating that they possess the symmetry of Mo sublattice. Moreover, the center of these protrusions is exactly on the position of the atoms in Mo layer and no visible lattice distortions are observed at the Cr-doped sites (Figures S12 and S13, Supporting Information). These results are consistent with the above STEM observations and EDS mappings, confirming that these Cr atoms are substitutional dopants in the lattice rather than surface adatoms. By visulizing the surface by STM, Figure 3i,j gives atomic level evidence of the density and uniform distribution of Cr dopants in the samples with different doping concentration. The atomic fraction of Cr (protrusions) extracted from the STM figure is generally consistent with the results extracted from EDS (Figure S14, Supporting Information). We also occasionally observed a very small amount of Cr adatoms on the surface. In sharp contrast to substitutional Cr, they locate in the hollow sites rather than Mo lattice sites and show isotropic round configuration with a much larger height of 1.56 Å (Figure S12, Supporting Information).

It is known that the Cr dopants can induce magnetic moments in the host. The interaction between itinerant electrons and localized magnetic moments becomes stronger with more dopants, giving rise to enhanced spin-flip scattering.[29,30] Therefore, the widely tunable uniform Cr doping opens up possibilities to tailor the properties of 2D Mo_2C superconductors

at macroscopic scale. We first conducted the low-temperature transport measurements on 2D Mo_2C crystals with different substitutional Cr concentration. **Figure 4**a shows a scanning electron microscope (SEM) image of a typical four-terminal Cr-doped Mo_2C device. The temperature dependence of the resistance of 2D Mo_2C crystals with four different Cr concentration (2.7, 9.4, 40.9, and 46.9 at%) is shown in Figure 4b for the temperatures below 60 K and zero magnetic field. All samples exhibit a metallic behavior at higher temperatures, but differ greatly at lower temperatures. Compared to the undoped pristine Mo_2C,[26,31–33] whose superconductivity is robust with critical temperature (T_c) ranging from 3 to 4 K, the sample with the lowest doping content (2.7 at%) exhibits still well-defined superconducting transition behavior but an obvious decrease in critical temperature ($T_c = 2.5$ K), indicating the suppression of superconductivity due to magnetic dopant effect. With increasing the amount of Cr dopant, no superconducting transition is observed down to 1.8 K, indicating a strong pair-breaking effect. The resistance shows a nonmonotonic temperature dependence at low temperature region, exhibiting a distinct upturn for temperatures below ≈ 40 K, which gradually become more pronounced with higher doping level. In the upper inset of Figure 4b, we show the normal-state sheet resistance (at 20 K) of samples with different Cr doping levels. It is seen that the sheet resistance rises monotonously with Cr doping, demonstrating the enhanced scattering arising from magnetic impurities.

Figure 4c displays temperature-dependent resistance of 2D Mo_2C crystals with 46.9 at% Cr. It is worth nothing that the resistance upturn gradually saturates at the lowest temperatures, a characteristic feature of the Kondo scattering arising from the magnetic moments. In the Kondo effect,[29,30] the antiferromagnetic coupling between itinerant electrons and localized magnetic moments screens the impurity spins, manifesting in the gradually saturated resistance upturn at lower temperatures. In order to quantitatively extract key parameter of the Kondo temperature, we analyzed the measured result using a simplified Kondo model, in which the temperature-dependent resistance can be described as[34]

$$R(T) = R_0 + qT^2 + pT^5 + R_K(0K)\left[T_K^{'2}/(T^2 + T_K^{'2})\right]^s \quad (1)$$

where R_0 is the residual resistance, and the T^2 and T^5 terms indicate the contributions of electron–electron and electron–phonon interactions, respectively. The last term is related to the Kondo effect with $T_K^{'} = T_K/(2^{1/s} - 1)^{1/2}$, where T_K is the effective Kondo temperature and $s = 0.225$ for a single spin impurity system according to the numerical renormalization group theory.[35,36] The data are well described using Equation (1), and fitting curve is depicted as a red line in Figure 4c. The obtained fitting parameters are $R_0 = 17.49$ Ω, $q = 2.61 \times 10^{-5}$ Ω K^{-2}, $p = 2.43 \times 10^{-10}$ Ω K^{-5}, $T_K = 22.2$ K. In the inset of Figure 4c, we plot the values of the Kondo temperatures T_K extracted from the fits for samples with three Cr concentration (9.4, 40.9, and 46.9 at%). It is seen that T_K exhibits a steady growth with increasing doping level, revealing a positive correlation between the strength of the induced Kondo effect and the quantity of magnetic elements.
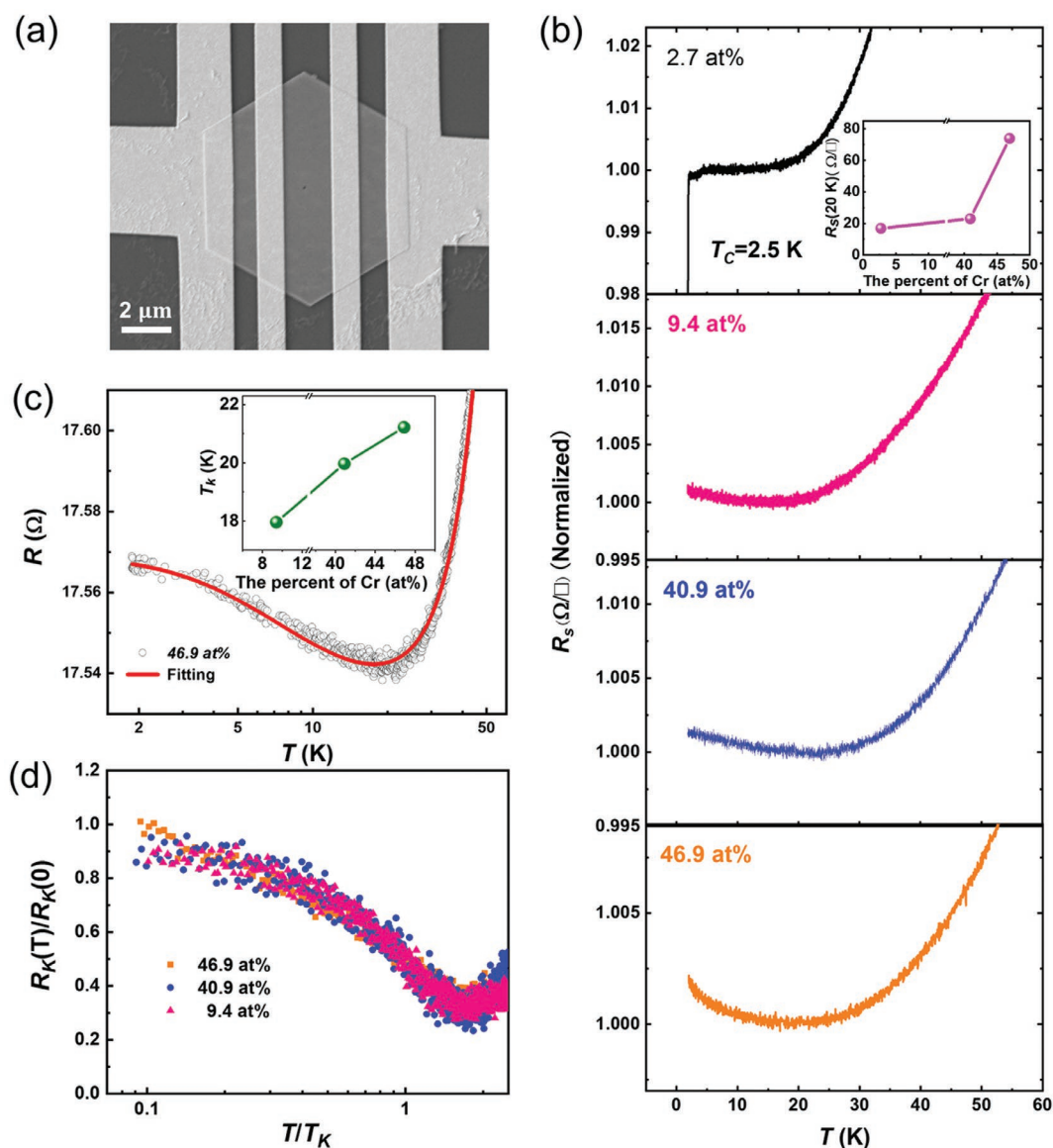
ADVANCED
SCIENCE NEWS

www.advancedsciencenews.com

ADVANCED
MATERIALS

www.advmat.de

Figure 4. Transport study and macroscopic Kondo effect in 2D Cr-doped Mo_2C flakes with different Cr concentrations. a) SEM image of a four-terminal device. The electrodes consist of Ti/Au bilayer span across the hexagonal Mo_2C flakes. b) Evolution of the temperature-dependent normalized sheet resistance with increasing Cr concentration (2.7 at%, 9.4 at%, 40.9 at%, and 46.9 at%). For clarity, the sheet resistance curves were normalized to the saturated region close to resistance drop for the doping content of 2.7 at%, while for 9.4 at%, 40.9 at%, and 46.9 at%, to the resistance minimum. The Cr dopants drastically alter the transport properties, transforming the superconducting into an upward resistance behavior. The inset shows the doping concentration-dependence of normal-state sheet resistance. c) Temperature dependence of resistance from a Mo_2C flake with 46.9 at% Cr and the corresponding fit with Equation (1) (red solid line). The inset depicts the evolution of T_K with Cr doping level. d) Universal Kondo behavior of the normalized resistivity R_K $(T)/R_K$ (0 K) versus T/T_K measured at different doping levels.

To further verify the Kondo scenario, we examined the empirical temperature-dependent Kondo resistance, $R_K(T) = R_K(0K)[T_K'^2 / (T^2 + T_K'^2)]^s$, which has a universal scaling function by rewriting as the following form

$$\frac{R_K(T)}{R_K(0K)} = \left[\frac{1}{\left(\left(T/T_K \right)^2 \times \left(2^{1/s} - 1 \right) + 1 \right)} \right]^s \tag{2}$$

In Figure 4d, we replotted the $R(T)$ curves obtained with three different Cr concentration (9.4, 40.9, and 46.9 at%) to

a normalized form by Equation (2), that is, the plot of scaled resistance $R_K(T)/R_K(0 K)$ against T/T_K. The experimental curves at different doping levels fall onto a single curve as a function of T/T_K at $T < T_K$, as expected for the universal Kondo behavior. At higher temperatures, the observed deviation can be attributed to the phonon scattering.

In order to understand the competition between the Kondo effect and the superconductivity at microscopic scale, STM/ scanning tunneling spectroscopy (STS) measurements were carried out. The Kondo resonance is a correlation of the conduction band electrons of a metal host with the unpaired electrons
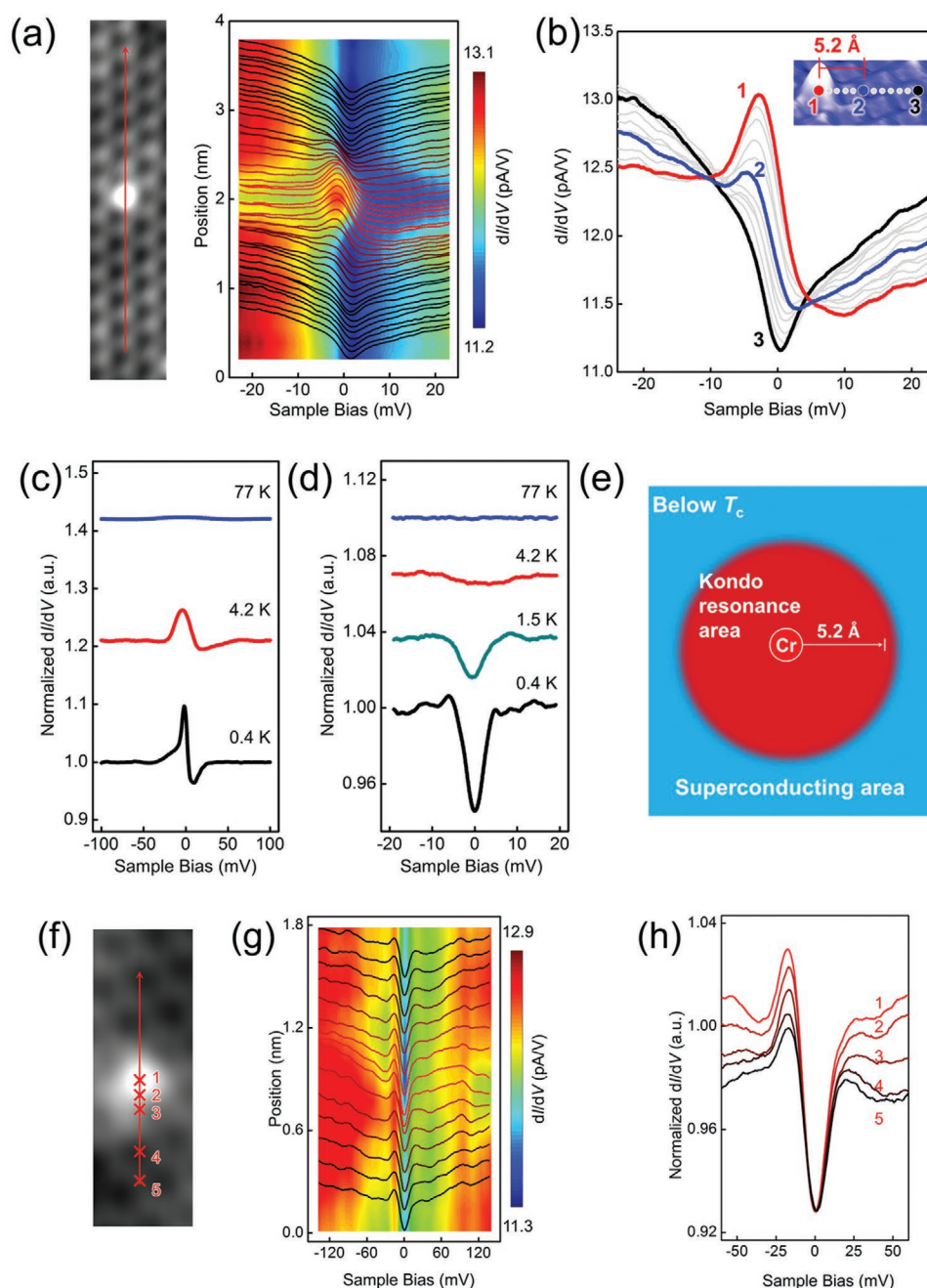
Figure 5. STM/STS measurements on the superconductivity and Kondo effect in 2D Cr-doped Mo_2C crystals. a) STM image (left) of 2.7 at% Cr-doped Mo_2C and a series of dI/dV spectra (right) measured along the red line. A distinct peak is observed on the Cr-doped site near the Fermi energy level (E_F). b) Representative dI/dV spectra taken at different lateral positions from the center of an isolated Cr monomer ($V_s = 15$ mV, $I_t = 0.25$ nA, $T = 0.4$ K). Inset: the side view of a Cr monomer. c,d) Temperature dependence of dI/dV spectra measured in the center (c) of and away from (d) the Cr dopant, respectively. e) Schematic illustration of the coexistence of Kondo resonance and the superconducting region at sufficiently low temperature and diluted doping level. f,g) STM image of 9.4 at% Cr-doped Mo_2C (f) and a series of dI/dV spectra measured along the red line (g). A distinct peak with similar strength is observed in the center of and away from the Cr dopant near the Fermi energy level (E_F). h) Representative normalized dI/dV spectra taken at different lateral positions from the center of an isolated Cr monomer ($V_s = 15$ mV, $I_t = 0.25$ nA, $T = 4.2$ K), showing the evolution of Kondo peak and trough.

of the magnetic impurity. Due to spin-flip scattering processes, a many electron singlet state is formed and enhances the local density of states (LDOS) near the Fermi energy (E_F) at the site of the magnetic impurity.[37] Herein, the Kondo effect was first investigated in 2.7 at% Cr-doped Mo_2C crystal. As shown in

Figure 5a, a series of dI/dV spectra were taken along the red line (left panel) at 0.4 K, and both the resulting color plot and the curves of dI/dV spectra are displayed in the right panel. We can see that the characteristics of the spectral curves change dramatically when the tip traversing the Cr impurity, i.e., from a dip to

a distinct DOS peak near E_F. As shown in Figure 5b, the Kondo resonance becomes weaker and weaker from the center to the edge of the Cr atom, and vanishes at a distance of about 5.2 Å. By fitting our data with Fano equation, a Kondo temperature T_K of ≈ 25 K is obtained (Figure S15a, Supporting Information), which is qualitatively consistant with the results of transport measurements at various doping levels (around 20 K). dI/dV spectra acquired at the top of single Cr dopant are displayed in Figure 5c, which were measured at different temperatures. A typical Kondo peak can be seen obviously at 0.4 K, and as the temperature increases, this peak became broader and lower at 4.2 K. Eventually, the signs of Kondo scattering totally vanished at the temperature of 77 K, which is much higher than T_K (around 20 K).

It is worth noting that, 2.7 at% Cr-doped 2D Mo_2C crystal still exhibits a superconducting transition temperature $T_c = 2.5$ K. As shown in Figure 5a,b, the corresponding dI/dV spectra measured away from the surface Cr protrusion exhibit a DOS suppression near the E_F at 0.4 K, and the normalized curves display a clear signature of a well-defined superconducting energy gap. This superconducting energy gap can be well fitted with the BCS Dynes formula (Figure S15b, Supporting Information). The temperature evolution of these dI/dV curves are shown in Figure 5d, in which the superconducting gap vanished near 2 K, fitting well with the T_c deduced in the transport measurements at this doping level (Figure 4b). Therefore, for such 2D Mo_2C with low doping level (2.7 at% Cr), there is an obvious competition between the Kondo and superconductivity when the temperature is below T_c, i.e., the suppression of the superconductivity by magnetic impurity. As shown in the schematic diagram (Figure 5e), the superconductivity of Mo_2C will be destroyed in the region within a radius of ≈ 5 Å from the center of Cr dopants. In such low doped sample (2.7 at% Cr), the distance of neighboring Cr dopants is large than 1 nm (Figure 3f) and therefore, the whole 2D Mo_2C sample still exhibits clear superconducting behavior under transport measurements. It should be noted that the $R(T)$ curves for 2.7 at% Cr-doped sample do not show an obvious resistance upturn at low temperatures (Figure S16, Supporting Information), which is a transport characteristic feature of the Kondo effect. However, these transport results do not contradict STM observations. It is known that the transport measurements reveal the manifestation of the charge scattering on the macroscale, while STM is a local probe on an atomic scale. For low doped samples, the Kondo scattering contribution to the resistance is strongly reduced due to diluted Cr dopants.

Figure 5f, g shows STM image and a series of dI/dV spectra in the center of and away from Cr dopants in 9.4 at% Cr doped Mo_2C crystals at a higher temperature (4.2 K). It is worth noting that the Kondo resonance with a considerable strength maintains away from Cr dopants (≥ 5.2 Å) (Figure 5h). This result suggests that different from the low doping level sample, the density of Cr atoms entering in the lattice for 9.4 at% Cr-doped Mo_2C crystals has reached to a value that can destroy the whole superconductivity rather than the local superconductivity remaining in the regions away from Cr atoms. Therefore, as the transport measurement results shown above, the superconductivity disappears in Cr-doped Mo_2C crystals with a doping level ≥ 9.4 at% even at 1.8 K.

Combining transport measurements and STM/STS results, we address the tunable competition of superconducting host

and magnetic impurities in 2D Mo_2C superconducting crystals. The Cr dopants introduce magnetic moments to Mo_2C, resulting in pair-breaking effect in the presence of spin-flip scattering and gradually destroying long-ranged superconducting order coherence. For low doped samples, the global superconductivity is still preserved, and the spin scattering contribution to the resistance is strongly reduced due to diluted Cr dopants. With increasing doping level, the broader spatially distributed Cr atoms, accompanied by hybridization between local spin and conduction electrons, destroy the superconductivity and set in global Kondo singlet states. As a result, the Kondo effect dominates the transport process leading to a resistance upturn at low temperatures.

In summary, we report the controlled and uniform lattice substitution of magnetic Cr in 2D superconducting Mo_2C crystals with a Cr concentration from 2.7 to 46.9 at% by CVD with Cr–Mo compound precursor, which enables the tuning of the competition of the 2D superconductivity and the Kondo effect in the whole sample rather than the observation at localized sites as reported previously. With such materials, the doping level effect on the interplay and evolution between superconductivity and the Kondo effect is revealed. Different from traditional CVD methods, our CVD method with doping-element-containing compound precursor allows subtle control of doping level of 2D materials without changing their original crystal structure, which provides a general route for the synthesis of a series of 2D materials with widely tunable doping levels. Such new materials will open up the possibilities for the investigation of many novel properties and applications that are absent for the pristine materials.

Experimental Section

Fabrication of Ultrathin Cr-Doped Mo_2C Crystals: Cr film was first deposited onto the surface of Mo foil (Alfa Aesar, 99.95% in purity, 100 μm in thickness) by magnetron sputtering. Then, a Cu foil (Alfa Aesar, 99.5% purity, 12.5 μm thick) was cut into pieces of 5×5 mm^2 and covered on the top of the Cr/Mo substrate. The obtained Cu/Cr/Mo substrate was placed in a quartz tube (25 mm outer diameter, 22 mm inner diameter) equipped in a horizontal tube furnace (Lindberg Blue M, TF55030C), and annealed at 1070 °C under H$_2$ (200 sccm) for 2 h to form a thin layer of Cr–Mo alloy sandwiched between Cu and Mo layers. Subsequently, a CH$_4$ flow of 0.35 sccm was introduced into the reaction tube to initiate the growth of 2D Cr-doped Mo_2C crystals. After 3–8 min growth, the sample was quickly removed from the high-temperature zone and cooled down to room temperature.

Transfer of Cr-Doped Mo_2C Crystals: The transfer process is similar to the transfer of CVD-grown pristine 2D Mo_2C crystals as reported in our previous work.[26] An ultrathin poly(methyl methacrylate) (PMMA, Mw = 960 000, 4 wt% in ethyl lactate) layer was first deposited on the Cr-doped Mo_2C crystals grown on Cu/Cr/Mo substrate by spin coating at 5000 rpm. for 60 s and then cured at 130 °C for 10 min. Subsequently, the PMMA/Cr-doped Mo_2C/Cu/Cr/Mo stack was immersed in a 0.2 M (NH$_4$)$_2$S$_2$O$_8$ solution at 70 °C for 20 min to remove the Cu layer. After etching, the separated PMMA/Cr-doped Mo_2C stack was cleaned with deionized water to remove the residual ions and then stamped onto SiO$_2$/Si substrate or TEM grid and cured at 110 °C for 10 min. Finally, the PMMA layer was removed by hot acetone at 65 °C to obtain clean 2D Cr-doped Mo_2C crystals.

Structure Characterization: The morphology of ultrathin Cr-doped Mo_2C crystals was characterized by optical microscopy (Nikon LV 100D), and the thickness and surface roughness were characterized by AFM (Mutil Mode VIII). The crystal structure, chemical composition and quality were charaterized by TEM. In detail, bright-field images and

**ADVANCED
SCIENCE NEWS**

www.advancedsciencenews.com

**ADVANCED
MATERIALS**

www.advmat.de

SAED patterns were taken by TEM (FEI Tecnai T12, 120 kV), and atomic-level HAADF-STEM images and EDS maps were obtained from 300 kV STEM (FEI Titan Cubed Themis G2 300). The element distributions in the samples were characterized by SIMS (ION TOF-SIMS V). A Bi ion beam (30 kV) was used to obtain the element maps in the lateral size. A strong O_2 ion beam (2 kV) was used to etch away the metal substrate to obtain the depth profile of various elements in the substrate, while a weak O_2 ion beam (250 V) sputtering was used to obtain subtle depth profile of various elements in the Cr-doped Mo_2C crystals. The 3D simulation for element distribution was obtained directly by SIMS system. Raman mapping was performed to confirm the uniformity of Cr-doped Mo_2C crystal at the microscale by using Raman spectroscopy (WITec Alpha 300R). The laser wavelength is 633 nm.

Device Fabrication and Transport Measurements: After CVD growth, ultrathin Mo_2C crystals with different Cr concentration were transferred onto SiO_2/Si substrate and located by optical microscopy. Four-terminal devices were fabricated by standard electronic beam lithography followed by electronic beam evaporation process with Ti/Au (5/90 nm) bilayer. The electrical measurements were performed in a Physical Property Measurement System (Quantum Design DynaCool) with a base temperature of 1.8 K and magnetic fields of up to 9 T applied perpendicular to the plane of the crystal. For the R–T curves, a standard lock-in technique was used by applying a small AC excitation current in the range of 0.1–1 μA at a frequency of ≈17.77 Hz, and measuring the AC voltage with Stanford Research Systems SR830.

STM/STS Characterization: The as-grown ultrathin Mo_2C crystals with different Cr concentrations, along with their Cu/Cr/Mo substrate, were first transferred into an ultrahigh vacuum (UHV) chamber of the STM system (USM-1300 from UNISOKU) and degassed at ≈300 °C for 3 h with a base pressure better than 5×10^{-10} Torr. The degassed samples were then transferred into an STM scanning chamber for in situ measurement in the UHV and low-temperature environment. All the STM images were measured at the constant-current mode using an electrochemically etched tungsten tip, and the dI/dV spectra were acquired by the lock-in technique. Lateral dimensions of the STM images were calibrated by Si(111)-(7×7) and Au(111) surfaces, and the superconducting gap structures appeared in dI/dV spectra were calibrated on the surface of bulk Pb.

Supporting Information

Supporting Information is available from the Wiley Online Library or from the author.

Conflict of Interest

The authors declare no conflict of interest.

[1] K. S. Novoselov, A. Mishchenko, A. Carvalho, A. H. Castro Neto, *Science* **2016**, *353*, aac9439.

[2] C. Tan, X. Cao, X.-J. Wu, Q. He, J. Yang, X. Zhang, J. Chen, W. Zhao, S. Han, G.-H. Nam, M. Sindoro, H. Zhang, *Chem. Rev.* **2017**, *117*, 6225.

[3] A. K. Geim, K. S. Novoselov, *Nat. Mater.* **2007**, *6*, 183.

[4] X. Wang, G. Sun, P. Routh, D. H. Kim, W. Huang, P. Chen, *Chem. Soc. Rev.* **2014**, *43*, 7067.

[5] C. Tan, Z. Lai, H. Zhang, *Adv. Mater.* **2017**, *29*, 1701392.

[6] P. Luo, F. Zhuge, Q. Zhang, Y. Chen, L. Lv, Y. Huang, H. Li, T. Zhai, *Nanoscale Horiz.* **2019**, *4*, 26.

[7] L. Lin, J. Li, Q. Yuan, Q. Li, J. Zhang, L. Sun, D. Rui, Z. Chen, K. Jia, M. Wang, Y. Zhang, M. H. Rummeli, N. Kang, H. Q. Xu, F. Ding, H. Peng, Z. Liu, *Sci. Adv.* **2019**, *5*, eaaw8337.

[8] X. K. Kong, C. L. Chen, Q. W. Chen, *Chem. Soc. Rev.* **2014**, *43*, 2841.

[9] Y. Shi, K. K. Kim, A. Reina, M. Hofmann, L.-J. Li, J. Kong, *ACS Nano* **2010**, *4*, 2689.

[10] Y. Gong, Z. Liu, A. R. Lupini, G. Shi, J. Lin, S. Najmaei, Z. Lin, A. L. Elias, A. Berkdemir, G. You, H. Terrones, M. Terrones, R. Vajtai, S. T. Pantelides, S. J. Pennycook, J. Lou, W. Zhou, P. M. Ajayan, *Nano Lett.* **2014**, *14*, 442.

[11] J. T. Ye, Y. J. Zhang, R. Akashi, M. S. Bahramy, R. Arita, Y. Iwasa, *Science* **2012**, *338*, 1193.

[12] B. Li, T. Xing, M. Zhong, L. Huang, N. Lei, J. Zhang, J. Li, Z. Wei, *Nat. Commun.* **2017**, *8*, 1958.

[13] Y. Saito, T. Nojima, Y. Iwasa, *Nat. Rev. Mater.* **2017**, *2*, 16094.

[14] Y. Yu, F. Yang, X. F. Lu, Y. J. Yan, Y. H. Cho, L. Ma, X. Niu, S. Kim, Y. W. Son, D. Feng, S. Li, S. W. Cheong, X. H. Chen, Y. Zhang, *Nat. Nanotechnol.* **2015**, *10*, 270.

[15] C. Gong, L. Li, Z. Li, H. Ji, A. Stern, Y. Xia, T. Cao, W. Bao, C. Wang, Y. Wang, Z. Q. Qiu, R. J. Cava, S. G. Louie, J. Xia, X. Zhang, *Nature* **2017**, *546*, 265.

[16] B. Huang, G. Clark, E. Navarro-Moratalla, D. R. Klein, R. Cheng, K. L. Seyler, D. Zhong, E. Schmidgall, M. A. McGuire, D. H. Cobden, W. Yao, D. Xiao, P. Jarillo-Herrero, X. Xu, *Nature* **2017**, *546*, 270.

[17] A. A. Abrikosov, L. P. Gor'kov, *Sov. Phys. JETP* **1961**, *12*, 1243; *Zh. Eksp. Teor. Fiz.* **1961**, *39*, 1781.

[18] E. Müller-Hartmann, J. Zittartz, *Phys. Rev. Lett.* **1971**, *26*, 428.

[19] S. H. Ji, T. Zhang, Y. S. Fu, X. Chen, X. C. Ma, J. Li, W. H. Duan, J. F. Jia, Q. K. Xue, *Phys. Rev. Lett.* **2008**, *100*, 226801.

[20] G. C. Ménard, S. Guissart, C. Brun, S. Pons, V. S. Stolyarov, F. Debontridder, M. V. Leclerc, E. Janod, L. Cario, D. Roditchev, P. Simon, T. Cren, *Nat. Phys.* **2015**, *11*, 1013.

[21] K. J. Franke, G. Schulze, J. I. Pascual, *Science* **2011**, *332*, 940.

[22] S. Nadj-Perge, I. K. Drozdov, J. Li, H. Chen, S. Jeon, J. Seo, A. H. MacDonald, B. A. Bernevig, A. Yazdani, *Science* **2014**, *346*, 602.

[23] B. Jäck, Y. Xie, J. Li, S. Jeon, B. A. Bernevig, A. Yazdani, *Science* **2019**, *364*, 1255.

[24] D. J. Chakrabarti, D. E. Laughlin, *Bull. Alloy Phase Diagrams* **1984**, *5*, 59.

[25] P. R. Subramanlan, D. E. Laughlin, *Bull. Alloy Phase Diagrams* **1990**, *11*, 169.

[26] C. Xu, L. Wang, Z. Liu, L. Chen, J. Guo, N. Kang, X.-L. Ma, H.-M. Cheng, W. Ren, *Nat. Mater.* **2015**, *14*, 1135.

[27] Z. Zhang, H. Gedeon, Z. Cheng, C. Xu, Z. Shao, H. Sun, S. Li, Y. Cao, X. Zhang, Q. Bian, L. Liu, Z. Liu, H.-M. Cheng, W. Ren, M. Pan, *Nano Lett.* **2019**, *19*, 3327.

[28] R.-L. Lo, K.-i. Fukui, S. Otani, Y. Iwasawa, *Surf. Sci. Lett.* **1999**, *440*, L857.

[29] J. Kondo, *Prog. Theor. Phys.* **1964**, *32*, 37.

[30] P. Nozières, *J. Low Temp. Phys.* **1974**, *17*, 31.

[31] D. Geng, X. Zhao, L. Li, P. Song, B. Tian, W. Liu, J. Chen, D. Shi, M. Lin, W. Zhou, K. P. Loh, *2D Mater* **2016**, *4*, 011012.

[32] L. Wang, C. Xu, Z. Liu, L. Chen, X. Ma, H.-M. Cheng, W. Ren, N. Kang, *ACS Nano* **2016**, *10*, 4504.

[33] S. Song, L. Wang, C. Xu, H.-M. Cheng, W. Ren, N. Kang, *IEEE Trans. Magn.* **2017**, *53*, 7100404.

[34] M. Lee, J. R. Williams, S. Zhang, C. D. Frisbie, D. Goldhaber-Gordon, *Phys. Rev. Lett.* **2011**, *107*, 256601.

[35] T. A. Costi, A. C. Hewson, V. Zlatic, *J. Phys. Conden. Matter* **1994**, *6*, 2519.

[36] D. Goldhaber-Gordon, J. Göres, M. A. Kastner, H. Shtrikman, D. Mahalu, U. Meirav, *Phys. Rev. Lett.* **1998**, *81*, 5225.

[37] N. Knorr, M. A. Schneider, L. Diekhoner, P. Wahl, K. Kern, *Phys. Rev. Lett.* **2002**, *88*, 096804.